Marquette University

e-Publications@Marquette

Biological Sciences Faculty Research and Publications

Biological Sciences, Department of

2-4-2019

Dynamics and Selective Remodeling of the DNA-binding Domains of RPA

Nilisha Pokhrel
Marquette University

Colleen C. Caldwell
University of Iowa

Elliot I. Corless
Marquette University

Emma A. Tillison
Marquette University

Joseph Tibbs
University of Northern Iowa

See next page for additional authors

Follow this and additional works at: https://epublications.marquette.edu/bio_fac

Part of the Biology Commons

Authors

Nilisha Pokhrel, Colleen C. Caldwell, Elliot I. Corless, Emma A. Tillison, Joseph Tibbs, Nina Jocic, S. M. Ali Tabei, Marc S. Wold, Maria Spies, and Edwin Antony

Biology Faculty Research and Publications/College of Arts and Sciences

Dynamics and Selective Remodeling of the DNA-binding Domains of RPA

Nilisha Pokhrel
Department of Biological Sciences, Marquette University, Milwaukee, WI
Colleen C. Caldwell
Department of Biochemistry, Carver College of Medicine, University of Iowa, Iowa City, IA
Elliot I. Corless
Department of Biological Sciences, Marquette University, Milwaukee, WI
Emma A. Tillison
Department of Biological Sciences, Marquette University, Milwaukee, WI
Joseph Tibbs
Department of Physics, University of Northern Iowa, Cedar Falls, IA
Nina Jocic
Department of Biochemistry, Carver College of Medicine, University of Iowa, Iowa City, IA
Department of Physics, University of Northern Iowa, Cedar Falls, IA
S. M. Ali Tabei
Department of Physics, University of Northern Iowa, Cedar Falls, IA
Marc S. Wold
Department of Biochemistry, Carver College of Medicine, University of Iowa, Iowa City, IA
Maria Spies

Department of Biochemistry, Carver College of Medicine, University of Iowa, Iowa City, IA

Edwin Antony

Department of Biological Sciences, Marquette University, Milwaukee, WI

Abstract

Replication protein A (RPA) coordinates important DNA metabolic events by stabilizing single-stranded DNA (ssDNA) intermediates, activating the DNA-damage response and handing off ssDNA to the appropriate downstream players. Six DNA-binding domains (DBDs) in RPA promote high-affinity binding to ssDNA yet also allow RPA displacement by lower affinity proteins. We generated fluorescent versions of *Saccharomyces cerevisiae* RPA and visualized the conformational dynamics of individual DBDs in the context of the full-length protein. We show that both DBD-A and DBD-D rapidly bind to and dissociate from ssDNA while RPA remains bound to ssDNA. The recombination mediator protein Rad52 selectively modulates the dynamics of DBD-D. These findings reveal how RPA-interacting proteins with lower ssDNA binding affinities can access the occluded ssDNA and remodel individual DBDs to replace RPA.

Main

In eukaryotic cells, RPA binds to transiently exposed ssDNA and serves as a hub protein to coordinate DNA replication, recombination, repair and telomere maintenance[1,2]. The cellular functions of RPA rely on its high ssDNA-binding affinity and its ability to physically interact with over two dozen DNA-processing enzymes and to correctly position these enzymes on complex DNA structures. The precise mechanisms by which RPA functions in many contexts and how RPA differentiates among multiple DNA metabolic events is a long-standing puzzle[1,3]. RPA is heterotrimeric, flexible and modular in structure. It is composed of three subunits, RPA70, RPA32 and RPA14 (Fig. 1a,b), which harbor six oligonucleotide/oligosaccharide-binding folds (labeled A through F). We refer to the DNA-binding oligonucleotide/oligosaccharide-binding folds as 'DBDs' (Fig. 1b). RPA binds to ssDNA with sub-nanomolar affinity but can be displaced by DNA-binding proteins with much lower DNA-binding affinity. Recent studies have suggested that the RPA–ssDNA complex is relatively dynamic[4,5,6], positing a selective dissociative mechanism where by not all DBDs are stably bound to the DNA, whereas microscopic dissociation of individual DBDs occurs.

Fig. 1: Non-canonical amino acid–based fluorescent RPA molecules report on individual DBD dynamics.
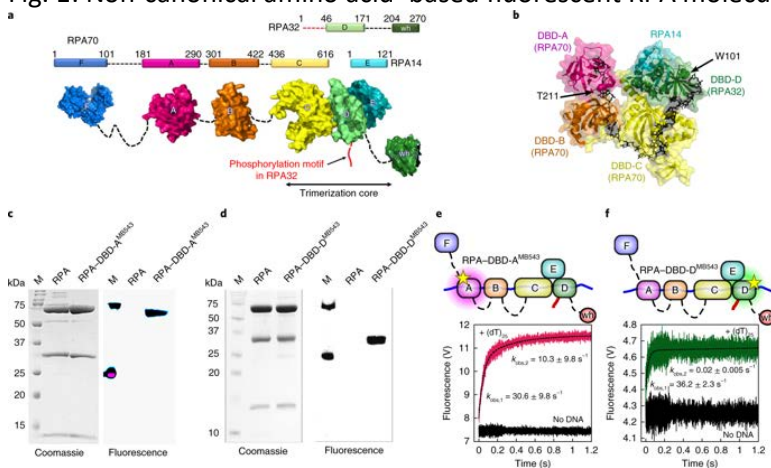
a, The residue numbers for the three RPA subunits and their respective DBDs (A–F) are denoted. The winged-helix (wh) domain in RPA32 and DBD-F in RPA70 mediate interactions with RIPs. The N terminus of RPA32 that is phosphorylated is shown in red. Crystal structures of the ordered domains are shown as surface representations with intervening disordered linkers as dotted lines (black). DBD-C, DBD-D and RPA14 interact to form the

trimerization core. **b**, Crystal structure of the DBDs of *Ustilago maydis* RPA bound to ssDNA (PDB 4GNX). Residues T211 in DBD-A and W101 in DBD-D are sites where 4-azidophenylalanine (4-AZP) is incorporated (residue numbering in *S. cerevisiae* RPA). The bound ssDNA is shown as sticks (black). **c,d**, Coomassie and fluorescence imaging of RPA complexes labeled with MB543 at either DBD-A or DBD-D. Only the fluorescently labeled domains are visualized by fluorescence imaging, suggesting site-specific labeling of each domain. **e,f**, Binding of RPA–DBD-A[MB543] and RPA–DBD-D[MB543] to ssDNA was analyzed by monitoring the change in MB543 fluorescence. A robust change in fluorescence depicts engagement of specific DBDs onto ssDNA. Data were fit and analyzed as described in Methods. Values depicted in **e**,**f** represent the mean and s.e.m. from *n* = 3 independent experiments. Uncropped gel images of **c,d** are shown in Supplementary Dataset 1.

In all existing models of RPA function, DBD-A and DBD-B are assigned as high-affinity DBDs. Purified DBD-A, DBD-B and DBD-A/DBD-B constructs bind ssDNA with equilibrium dissociation rate constant (K_d) values of 2 µM, 20 µM and 50 nM, respectively[7,8,9]. The trimerization core made up of DBD-C, DBD-D and DBD-E is considered to have a weaker ssDNA binding affinity (K_d > 5 µM)[10]. Additionally, mutational analysis of individual aromatic residues that interact with the ssDNA in either DBD-C or DBD-D show minimal perturbations in ssDNA binding affinity[6,11]. Paradoxically, in the crystal structure of the RPA–ssDNA complex (Fig. 1b), the ssDNA interactions of all four DBDs are similar, with DBD-C having more contacts with ssDNA bases than does DBD-A, DBD-B or DBD-D[12]. Thus, the exact nature of the contributions from each DBD to RPA function is probably complicated and may be influenced by the dynamics of DBD–ssDNA interactions.

Both the N terminus of RPA70 and the C terminus of RPA32 interact with distinct sets of RPA-interacting proteins (RIPs). During DNA processing, RIPs must displace RPA from ssDNA. Displacement may be achieved by modulation of the DNA-binding activity of specific DBDs within RPA. In such a model, a protein that exchanges for RPA does not dissociate all DBDs at once but displaces individual DBDs after gaining access to DNA that is transiently exposed by dissociation of a DBD. Moreover, if the RPA–ssDNA complex were to be considered a sequential, linear assembly of DBDs, as seen in the crystal structure, then, depending on the DBD first displaced, a downstream DNA-binding protein could be positioned at the 5' or 3' end of the RPA-occluded ssDNA.

The recombination mediator Rad52 is one example of a RIP. It belongs to a group of proteins that orchestrate homologous recombination and homology-directed DNA repair. *S. cerevisiae* Rad52 regulates recombination by facilitating replacement of RPA on ssDNA with the Rad51 nucleoprotein filament, an active species in homology search and DNA strand exchange[13,14,15,16]. Nucleation of the Rad51 filament is a slow and tightly controlled process, as Rad51 fails to compete for binding to ssDNA with RPA[17]. Thus, Rad52 must physically interact with both RPA and Rad51 to promote Rad51 filament nucleation. The mechanism by which Rad52 loads Rad51 onto the ssDNA is unclear, except that Rad51 filament formation is simultaneous with displacement of RPA from ssDNA and probably proceeds through a Rad52–RPA–ssDNA intermediate[17]. Within this complex, Rad52 was shown to stabilize the RPA–ssDNA interaction[18], further mystifying its assigned mechanism of action as a recombination mediator.

To determine how individual DBDs work in the context of the full-length protein and investigate how proteins such as Rad52 modulate RPA binding, we generated fluorescent forms of RPA containing a non-canonical amino acid that is labeled with the fluorescent dye MB543 in either DBD-A or DBD-D. When MB543 is positioned near the DNA-binding site, the fluorescence intensity of MB543 changes after binding to ssDNA occurs. Using direct measurements of full-length RPA carrying a fluorescently labeled DBD binding to and dissociating from ssDNA, we show that both DBD-A and DBD-D are highly dynamic, frequently binding to and dissociating from ssDNA. We also show that RPA–ssDNA complexes exist in at least four distinct conformational states offering differential access to the ssDNA within this complex. Rad52 interacts with the RPA–ssDNA complex and selectively

modulates the dynamics of DBD-D, preventing its full engagement with ssDNA and thereby opening the 3' end of the RPA-occluded sequence.

Results

Direct readout of DBD dynamics using non-canonical amino acids and fluorescence

Directly monitoring the dynamics (binding, dissociation or remodeling) of a single enzyme in multiprotein reactions remains technically challenging. To decipher how the DBDs of RPA function in the context of the heterotrimeric RPA complex, we labeled DBD-A or DBD-D (in RPA70 or RPA32, respectively; Fig. 1c,d) of *S. cerevisiae* RPA[19] with MB543, an environmentally sensitive fluorophore. Both fluorescently labeled RPA molecules are fully active for ssDNA binding with binding parameters and occluded binding site sizes typical of the wild-type RPA protein (Supplementary Note 1 and Supplementary Fig. 1). RPA labeled at domain A (RPA–DBD-A^{MB543}) or domain D (RPA–DBD-D^{MB543}) produces enhanced fluorescence after binding to ssDNA (Fig. 1e,f and Supplementary Fig. 2)[19].

The binding of RPA to ssDNA is a paradigm for reactions in which multiple DNA-binding proteins function together on a single DNA template. Knowledge of where, how and when each protein gains access to the DNA in this multi-enzyme milieu is fundamental to deciphering when and how specific DNA repair/recombination processes are orchestrated. Site-specific labeling with MB543 allows us to monitor the dynamics of individual DBDs in the context of the full-length RPA heterotrimer and in multiprotein reactions. We measured the DNA-binding kinetics for RPA–DBD-A^{MB543} and RPA–DBD-D^{MB543}, which provided direct readouts of each domain's engagement with ssDNA in the context of full-length RPA. RPA–DBD-A^{MB543}or RPA–DBD-D^{MB543} was rapidly mixed with ssDNA ((dT)$_{25}$), and the change in fluorescence was measured (Fig. 1e,f). After binding to ssDNA, both RPA–DBD-A^{MB543} and RPA–DBD-D^{MB543} produce a change in fluorescence intensity. The data for RPA–DBD-A^{MB543} are best described by a two-step model (with observed rate constants $k_{obs,1}$ = 30.6 ± 9.8 s^{-1} and $k_{obs,2}$ = 10.3 ± 9.8 s^{-1}), whereas intensity changes associated with RPA–DBD-D^{MB543} best fit a single-step DNA-binding model (k_{obs} = 36.2 ± 2.3 s^{-1}). The first rate in both models is similar and reflects the initial interaction of RPA with ssDNA. The second step for RPA–DBD-A^{MB543} possibly reflects a rearrangement of DBD-A, as has been observed in structural studies[20,21]. To probe the nature of these differences further, we performed these binding experiments as a function of increasing DNA concentration using (dT)$_{35}$, which provides enough space for engagement of all the DBDs of RPA (Fig. 2). While measurements of RPA–ssDNA interaction footprints under our buffer conditions yield occluded site sizes of ~20 nucleotides (nt) per RPA (Supplementary Fig. 1h), the modularity of the DBDs have been shown to produce occluded site sizes between 18 nt and 28 nt (ref. 22).

Fig. 2: DNA-binding dynamics of individual DBDs.
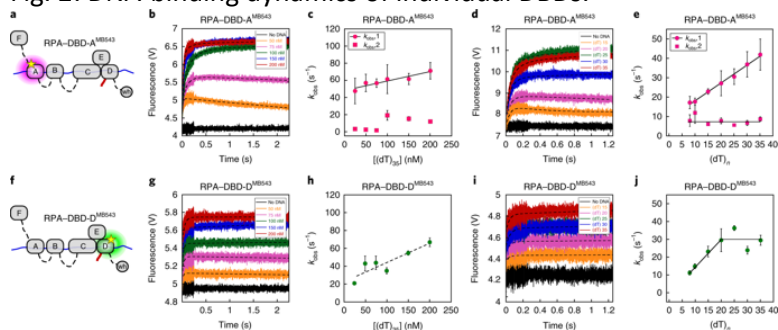
a,f, Cartoons depicting the binding of RPA–DBD-A^{MB543} or RPA–DBD-D^{MB543} to ssDNA and producing a change in fluorescence. b–e, Stopped-flow experiments carried out with increasing concentrations of (dT)$_{35}$ ssDNA (b,c) or with ssDNA of increasing length ((dT)$_n$, where 'n' indicates the length of the oligonucleotide) (d,e) capture the observed rates in fluorescence change for RPA–DBD-A^{MB543}. g–j, Stopped-flow analysis of RPA–DBD-D^{MB543}ssDNA-binding dynamics. The data for RPA–DBD-A^{MB543} are best fit using a two-step model, whereas the

data for RPA–DBD-D[MB543] fit to a one-step process, suggesting distinct DNA context–dependent changes in their dynamics. Error bars in panels **c,e,h,j** represent the mean and s.e.m. from n = 3 independent experiments.

The observed rate for the first association step for both RPA–DBD-A[MB543] and RPA–DBD-D[MB543] increases as a function of DNA concentration, yielding bimolecular binding rate constant (k_{on}) values ((1.1 ± 0.6) × 10^8 M^{-1} s^{-1} and (2.1 ± 0.4) × 10^8 M^{-1} s^{-1}, respectively; Fig. 2a–c, f–h). The second step, observed only for RPA–DBD-A[MB543], is not linear (Fig. 2c). This is consistent with a conformational rearrangement of DBD-A after the complex with ssDNA has been established and depends on the protein-to-DNA ratio in the reaction. Under conditions in which RPA is present in excess over ssDNA, we clearly observe biphasic binding and dissociation/rearrangement phases for RPA–DBD-A[MB543] (orange and pink traces in Fig. 2b) but not for RPA–DBD-D[MB543] (Fig. 2g). These data suggest that the dynamics of individual DBDs are not identical, possibly reflecting different functional roles.

FRET analysis confirms primary assessments of DBD–ssDNA dynamics

In the experiments described above, the change in fluorescence intensity arises from local environmental changes of the fluorophore after binding to the ssDNA. We suggest that changes in the MB543 fluorescence reflect changes in the electrostatic environment of the dye (Supplementary Fig. 2). To reaffirm that the accuracy of the dynamics we measured for each fluorescent DBD reflects ssDNA interactions, we used Förster resonance energy transfer (FRET) to capture DBD–ssDNA-binding kinetics. RPA binds to ssDNA with specific polarity where DBD-A is positioned closer to the 5' end of the ssDNA[12,23]. Similar to the MB543-labeled proteins, we generated Cy5-labeled RPAs in which either DBD-A or DBD-D was labeled with Cy5. We next performed FRET experiments with either 5'- or 3'-Cy3-end-labeled DNA [(dT)$_{34}$]. On 5'-Cy3 DNA, a high FRET signal is observed for RPA–DBD-A[Cy5] and a medium FRET state is captured for RPA–DBD-D[Cy5] (Supplementary Fig. 3a,b). In the corollary experiment with 3'-Cy3 DNA, a low FRET state for RPA–DBD-A[Cy5] and a high FRET state for RPA–DBD-D[Cy5] are observed (Supplementary Fig. 3c,d). These experiments are consistent with the expected 5'-to-3' polarity of RPA binding. Strikingly, the observed rate for the appearance of the RPA–DBD-D[Cy5] high FRET state (36 ± 2 s^{-1}; Supplementary Fig. 3d) agrees with the rate for change in fluorescence intensity of RPA–DBD-D[MB543] after binding to ssDNA (36.2 ± 2 s^{-1}; Fig. 1f). Similarly, the observed rate of 21 ± 1 s^{-1} for the appearance of the RPA–DBD-A[Cy5] high FRET state (Supplementary Fig. 3b) is probably a composite of the two observed phases captured in fluorescence-intensity changes of the RPA–DBD-A[MB543]–ssDNA complex ($k_{obs,1}$ = 30 s^{-1} and $k_{obs,2}$ = 10 s^{-1}; Fig. 1e). The FRET data affirm that the ssDNA-binding responsive fluorescence intensity enhancements reflect specific DBD–ssDNA interactions.

Differential effects of ssDNA length on DBD conformations

Since each DBD has varying footprints on ssDNA[12], we measured the DBD dynamics as a function of ssDNA length and found that the $k_{obs,1}$ increases as a function of ssDNA length for RPA–DBD-A[MB543] (Fig. 2d, e), whereas the same parameter saturated for RPA–DBD-D[MB543] at ~20 nt (Fig. 2i, j). On shorter DNA lengths, both binding and dissociation phases are clearly observed for RPA–DBD-A[MB543] (Fig. 2d, (dT)$_{15}$ and (dT)$_{20}$ traces); however, only a single binding phase for RPA–DBD-D[MB543] is observed with all ssDNA lengths (Fig. 2i). Since ssDNA and RPA are in molar equivalents in these experiments, the dissociation from shorter DNA probably occurs from intrasubunit competition among the four DBDs of RPA. DBD-F, DBD-A and DBD-B are considered the conformationally flexible half[24]. In contrast, DBD-C, DBD-D and DBD-E constitutively interact to form the trimerization core and are more conformationally rigid. We considered the possibility that the trimerization core might be outcompeting the more dynamic DBD-A (and possibly DBD-B) under conditions of excess RPA or when the length of the DNA is too short to accommodate all the DBDs. To test this scenario, we generated the RPA–FAB fragment containing DBD-F, DBD-A and DBD-B and labeled it with MB543 in DBD-A (RPA–FAB-A[MB543]). Stopped-flow measurement of DNA-binding kinetics of RPA–FAB-A[MB543] yield k_{on} = (1.0 ± 0.1) × 10^8 M^{-1} s^{-1} (Supplementary Fig. 4a–d), which is similar

to that measured for RPA–DBD-A^{MB543} ($(1.1 \pm 0.6) \times 10^8\,M^{-1}\,s^{-1}$; Fig. 2b,c), suggesting that DBD-A has a DNA-binding capacity intrinsically distinct from that of DBD-D and possibly other DBDs as well. Interestingly, RPA–FAB-A^{MB543} binds to ssDNA with monophasic kinetics under conditions of both excess protein and shorter DNA lengths (Supplementary Fig. 4b,c and Supplementary Note 2). This suggests competitive binding and rearrangements between the DBDs within full-length RPA when the binding sites on ssDNA are limiting. We propose that when only a short segment of ssDNA (($(dT)_{15}$ or $(dT)_{20}$) is available, DBD-A rapidly binds and dissociates, whereas DBD-D (and possibly the trimerization core) forms more stable, longer-lived complexes with ssDNA, thus outcompeting DBD-A from short ssDNA substrates. These data also suggest that the interactions of each DBD and the resulting conformations of the RPA–ssDNA complex are sensitive to the context of DNA encountered during various DNA metabolic processes in the cell.

Single-molecule analysis reveals the presence of multiple conformational states involving DBD-D and DBD-A

The ensemble stopped-flow experiments described above suggest that the terminal DBDs of RPA associate with ssDNA with different rates and that, after binding to ssDNA, RPA commences complex and dynamic rearrangement of its DBDs. Single-molecule total internal reflection microscopy (smTIRFM) was used to directly observe RPA–DBD-A^{MB543}and RPA–DBD-D^{MB543} binding to and dissociating from surface-tethered ssDNA in the context of the RPA heterotrimer. In the smTIRFM experiments, biotinylated ssDNA (66 nt) was tethered to the surface of the TIRFM flow cell (see Methods for details). The surface was illuminated with a 532-nm laser to excite the MB543 dye on fluorescent RPA molecules entering the evanescent field (Fig. 3a,b). Binding of a MB543-labeled RPA to surface-tethered ssDNA molecules generates a fluorescence signal at a particular location of the flow-cell surface. This signal persists until RPA dissociates or transitions to a dark state (and then dissociates) or until the dye photobleaches.

Fig. 3: Single-molecule analysis quantifies the conformational dynamics of DBDs and the effect of the recombination mediator Rad52.
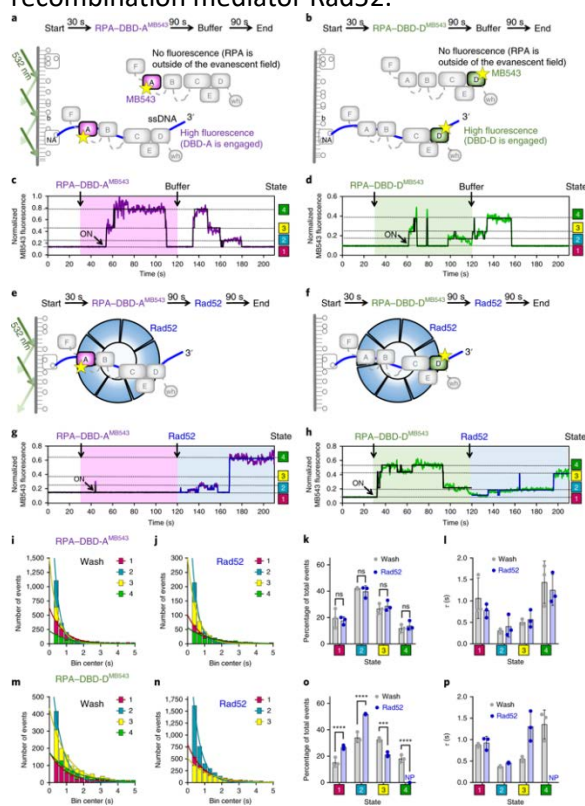
a,b, Experimental scheme for visualizing conformational dynamics of DBD-A and DBD-D. Binding of fluorescently labeled RPA to a surface-tethered ssDNA (purple line) brings the MB543 fluorophore within the evanescent field of TIRFM. NA, NeutrAvidin; b, biotin. **c,d**, Representative fluorescence trajectories for individual RPA–DBD-A[MB543]and RPA–DBD-D[MB543]molecules (purple lines and green lines, respectively). Black lines are the result of ebFRET fitting. Additional examples of representative trajectories are presented in Supplementary Datasets 2 and 3. **e,f**, Experimental scheme for visualizing the effect of Rad52 on the conformational dynamics of DBD-A and DBD-D. **g,h**, Representative fluorescence trajectories depicting conformational dynamics of the individual RPA–DBD-A[MB543]and RPA–DBD-D[MB543]molecules after the addition of Rad52. Additional trajectories are shown in Supplementary Datasets 5 and 6. **i,j**, Dwell-time histograms for the four fluorescent states obtained by the ebFRET fitting of RPA–DBD-A[MB543] trajectories from three independent experiments after buffer wash (**i**) and Rad52 wash (**j**). Before analysis, the trajectories were cut from 120 s to 210 s. Solid lines represent the single exponential fit. The data are summarized in Supplementary Table 1. **k**, Fractional visitation to each state available to RPA–DBD-A[MB543]alone (gray) and in the presence of Rad52 (blue). The two-way analysis of variance (ANOVA) suggests no significant differences between the visitation frequencies in the presence and absence of Rad52 ($P > 0.1$). **l**, Stability of each state available to RPA–DBD-A[MB543] alone (gray) and in the presence of Rad52 (blue). The data on the y axis are the lifetimes for the respective dwell-time distributions. **m–p**, The same analysis was carried out for RPA–DBD-D[MB543]. Only three fluorescence states were detected in the presence of Rad52. NP, not present. Statistical analysis is performed by ANOVA (***, $P = 0.0001$ and ****, $P < 0.0001$).

Several hundred molecules are observed in the field of view, each yielding a fluorescence trajectory (that is, a change in fluorescence in a particular location on the slide as a function of time)[25]. The trajectories allow measurement of binding and dissociation of individual RPA molecules. Moreover, fluorescence changes of the dye in the trajectory can also report on the presence of conformational states in the dye-decorated protein[26]. The experiments were carried out in three stages: first, the surface was observed for 30 s to confirm the absence of the non-protein-derived fluorescence spots; second, RPA–DBD-A[MB543] or RPA–DBD-D[MB543] was injected into the flow cell; finally, at 120 s, protein-containing solution was replaced with the buffer (Fig. 3a,b). The final step ensured that the observed changes in fluorescence could be attributed to single RPA molecules. Fluorescence trajectories were extracted from the recorded videos and were normalized (see Methodsand Supplementary Fig. 5). The resultant trajectories showed the dynamics within the RPA–ssDNA complex (Fig. 3c,d). Transitions between different fluorescence states persisted during the final segment of the experiment, suggesting that they truly reflect the conformational dynamics of individual RPA–ssDNA complexes. Notably, a surface-tethered RPA displayed essentially invariable, one-state fluorescence with only very rare excursions into a dark state (Supplementary Fig. 6a,b). Global analysis of normalized trajectories for the ssDNA-bound RPA–DBD-A[MB543] and RPA–DBD-D[MB543] was performed with ebFRET[27,28]. The number of trajectories and states in each experiment are summarized in Supplementary Table 1 and Supplementary Dataset 4. This analysis revealed that the fluorescence derived from both proteins best fit a four-state model, with state 1 corresponding to very low fluorescence and states 2–4 corresponding to increasing fluorescence enhancement (Fig. 3c,d). Segments of the trajectories between 120 s and 210 s, which can be attributed to the dynamics of a single bound RPA, were used in the quantification of the lifetimes and visitation frequencies for all states.

We attribute state 4 in each case to the RPA conformation in which the labeled domain is probably fully engaging the ssDNA, because in bulk experiments we observed an ssDNA-dependent fluorescence increase in the full-length RPA carrying the fluorophore and RPA–FAB-A[MB543](containing only DBD-A and DBD-B). To rule out the possibility that the lowest fluorescence state (state 1) followed by the reappearance of the fluorescence during the last 90 s of the experiment is due to the dissociation and rebinding of RPA, we substituted the buffer wash with a buffer supplemented with a high concentration of ssDNA. In the absence of additional RPA in the solution, the ssDNA competitor cannot strip the bound RPA from the DNA but can sequester all dissociated RPA

molecules[5]. As expected, the addition of ssDNA to the reaction chamber had no effect on the RPA fluorescence states (Supplementary Fig. [7] and Supplementary Table [2]).

We ruled out the possibility of photophysical effects as the source of the MB543 fluorescence states by repeating the experiments at three different powers of the excitation laser, as true conformational states should not display any trend in power dependence[26,29,30]. The data, summarized in Supplementary Fig. [6c,d] and Supplementary Table [3], show no change in the laser power dependence for any of the four states of RPA–DBD-D[MB543], thus confirming that this is the case. Additionally, the absence of distinct fluorescence states for RPA alone, with the exception of the infrequent visitation of the dimmest state, suggests that the observed states are induced by the interaction with ssDNA (Supplementary Fig. [6a,b]). The four fluorescence states and their dwell times were consistent between independent experiments, suggesting that the normalization scheme we developed yields reproducible results (Fig. [3k,l,o,p]). For both RPA–DBD-A[MB543] and RPA–DBD-D[MB543], states 1 and 4 were the most stable, with average dwell times around 1 s, compared to states 2 and 3, whose average dwell times were between 300 ms and 500 ms. As evident from the representative trajectories (Fig. [3c,d] and Supplementary Dataset 2 and 3), RPA spends substantial periods of time in states in which DBD-A or DBD-D is not fully engaged, providing a window of binding opportunity for proteins of lower affinity.

In addition, we found that the collective DNA-binding affinities of all DBDs produce stable RPA–ssDNA complexes. DBD-A and DBD-B have been canonically assigned as being responsible for high-affinity DNA binding of the RPA complex. By carrying out single-molecule experiments with RPA–FAB-A[MB543], we found that it forms a less-stable complex on ssDNA and readily dissociates (Supplementary Fig. [4e–h]). These findings agree with the results from the bulk stopped-flow experiments (Supplementary Fig. [8] and Supplementary Note [2]). Fluorescence trajectories recorded for RPA–FAB-A[MB543] were best fit with the three-state model (Supplementary Fig. [4f]). State 1 corresponded to free ssDNA, and its lifetime displayed a linear dependence on the RPA–FAB-A[MB543] concentration (Supplementary Fig. [4h]). States 2 and 3 were present in the bound state of RPA–FAB-A[MB543], whose two DBDs had been suggested to form a dynamic complex on the ssDNA[31]. The presence of only two fluorescence states in RPA–FAB-A[MB543] further confirms that the four states observed for the full-length RPA are not photophysical states inherent to the MB543 dye.

Rad52 selectively modulates DBD-D dynamics

To determine the mechanism by which the recombination mediator Rad52 remodels the RPA–ssDNA complex, RPA–DBD-A[MB543] or RPA–DBD-D[MB543] bound to the surface-tethered ssDNA in the smTIRFM experiments were challenged with Rad52 (Fig. [3e,f] and Supplementary Datasets 5 and 6). The final 90-s portions of the resulting trajectories were normalized and globally analyzed using ebFRET. Dwell times for each state were binned and fit to an exponential decay (Fig. [3i, j,m,n], Supplementary Dataset 4 and Supplementary Table [1]). RPA–DBD-A[MB543]trajectories after buffer wash or after Rad52 addition fit best to a four-state model with the same distribution of states and the same dwell times (Fig. [3i–l]). The trajectories collected for RPA–DBD-D[MB543] after Rad52 addition instead best fit a three-state model (Fig. [3m–p]). Attempts to fit these trajectories with a four-state model resulted in overfitting and overlapping states. Intensities of the three states of RPA–DBD-D[MB543] after Rad52 addition correspond to the three lowest states seen after the buffer wash, with the highest state being absent when Rad52 was present (Fig. [3h], blue shaded area). With RPA–DBD-D[MB543], state 4 is lost after Rad52 addition and state 3 occupancy decreases, whereas state 1 and state 2 occupancy increases (Fig. [3o]). This suggests that Rad52 selectively modulates the conformational dynamics of the RPA–ssDNA complex, reducing the engagement of DBD-D with ssDNA and providing access to the 3' end of the occluded ssDNA.

Formation of the RPA–ssDNA–Rad52 complex depends on physical interaction between RPA and Rad52, which is mediated by ssDNA and is confined to the middle region of the Rad52 C-terminal domain[32,33]. To test whether the modulation of DBD-D by Rad52 depends on interaction between the two proteins, we used human RAD52,

which resembles the yeast protein in all its activities but does not interact with yeast RPA[34]. We found that human RAD52 does not alter the four states of the interaction of RPA–DBD-D^{MB543} with DNA (Supplementary Fig. [9a–d]). Thus, the modulation of state 4 is specific for yeast Rad52 and therefore requires Rad52–RPA interaction. To highlight the importance of the interaction between Rad52 and ssDNA for modulating the RPA conformational dynamics, we performed an experiment in the presence of a Rad52 inhibitor, epigallocatechin (EGC) (Supplementary Fig. [9e–k]). EGC inhibits the DNA-binding activity of human RAD52[35] and yeast RAD52, but not that of RPA (Supplementary Fig. [9e–f]). We observed the four fluorescence states of RPA–DBD-D^{MB543} in the presence of Rad52 and EGC (Supplementary Fig. [9g–k] and Supplementary Table [4]). These data suggest that the loss of state 4 also depends on the DNA-binding activity of Rad52.

Discussion

Prior RPA binding models have been based on analysis of subcomplexes or mutations. In contrast, we have analyzed the dynamics of individual domains in the context of the full RPA–ssDNA complex. This analysis demonstrates that rather than being composed of 'high' and 'low' affinity domains, all DBDs transiently engage ssDNA with high affinity, but with differential dynamics. We also observe interplay between the flexible half of RPA (DBD-F, DBD-A and DBD-B) and the trimerization core. Thus, the RPA–ssDNA complex consists of an ensemble of domains that dynamically interact with ssDNA. This suggests that integration of these interactions results in an overall high affinity for ssDNA while facilitating diverse functions of RPA. Our data also suggest that the assembly of DBDs on ssDNA is not sequential but is instead the result of dynamic, independent interactions between connected DBDs and DNA.

RPA forms a complex with the recombination mediator Rad52[32,36]. RPA is in dynamic equilibrium on ssDNA, and Rad52 has been shown to increase the residence time of RPA on ssDNA[18]. The formation of 'early Rad52-bound' RPA and that of 'late Rad52-bound' RPA are proposed to play distinct roles during Rad51 filament formation and second-strand capture during homologous recombination[18]. The ability to observe the individual RPA DBDs binding to, and dissociating from, the ssDNA in real time permits a mechanistic description of RPA–ssDNA–Rad52 interactions. The RPA heterotrimer and the heptameric Rad52 ring have similar ssDNA-binding sites. Each Rad52 monomer contains an RPA-binding site, and RPA has two Rad52-binding sites per heterotrimer. Rad52 is believed to interact with the ssDNA backbone, while the DBDs of RPA, especially within the trimerization core, engage the bases. Our results show that stabilization of RPA by Rad52 is a result of both their physical interactions and their individual interactions with DNA. We therefore envision a ternary complex in which Rad52 and RPA interact with one another while both proteins are simultaneously bound to ssDNA. Selective modulation of DBD-D ssDNA engagement by Rad52 provides space for Rad52 to interact with ssDNA and stabilize the ternary complex, which then makes more extensive contacts with the ssDNA than RPA does on its own. By redistributing the ssDNA between RPA and Rad52, and by reducing the contacts between RPA and ssDNA, such selective remodeling by Rad52 may provide the Rad51 recombinase access to the 3′ end of RPA-occluded ssDNA while maintaining its interaction with RPA (Fig. [4]). Each Rad51 monomer binds to one monomer of Rad52 and to three nucleotides of ssDNA. Six Rad51 monomers are required to achieve a stable nucleation cluster[37], which amounts to 18 nucleotides of open ssDNA. This cannot be achieved without the help of a recombination mediator. When Rad52 binds to ssDNA-bound RPA, it modifies the dynamics of the DBD-D engagement. This provides a stretch of ssDNA of sufficient length to initiate Rad51 filament nucleation. We predict that recombination mediators in other species, including human BRCA2, may operate by a similar mechanism. The details of this mechanism, however, will depend on the intrinsic differences in nucleoprotein filament formation by human RAD51, which nucleates on ssDNA through dynamic association of RAD51 dimers[38] and grows from heterogeneous nuclei ranging in size from dimers to oligomers[39].

Fig. 4: Dynamics of RPA DBDs and modulation by Rad52.
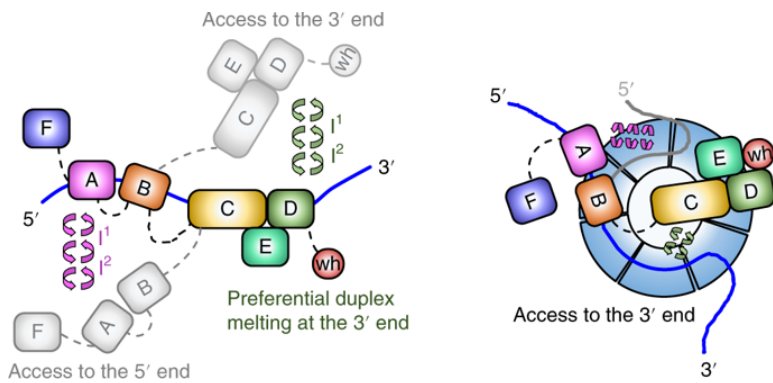
a, Sequential and directional arrangement of the DBDs allows RPA to occlude 20–30 nt of ssDNA (~20 nt under our experimental conditions; Supplementary Fig. 1). When RPA is in a stoichiometric complex with ssDNA, or when the ssDNA is in excess, the individual DBDs of RPA exist in a variety of distinct dynamic conformational DNA-bound states. Such conformational flexibility allows access to either the 5′ segment or the 3′ segment of the DNA to other proteins that function in downstream processes. The circular arrows represent the transitions between the multiple fluorescence states that we observe in the single-molecule experiments and that are implied by the bulk stopped-flow experiments. Note that while we illustrate the changes in the conformation of the RPA–ssDNA complex as movement of the DBDs, the same microscopically bound states may arise from ssDNA dissociating and moving away from the respective DBDs. **b**, The DBDs are also selectively modulated by RIPs such as Rad52. In this case, only the DNA-binding dynamics of DBD-D, and possibly the trimerization core, are influenced by Rad52. In the ternary RPA–ssDNA–Rad52 complex, the ssDNA is shared by RPA and Rad52, which also interact with one another. The ability of DBD-D and other RPA elements to contact the ssDNA near the 3′ end of the occluded sequence is constrained. Such selective DBD modulation may promote loading of Rad51 onto the 3′ end of the ssDNA during homologous recombination.

The myriad roles of RPA in DNA replication, repair and recombination are also a paradigm for reactions in which multiple DNA-binding enzymes function together on a single DNA template. Knowledge of where, how and when each enzyme gains access to DNA in this multi-enzyme milieu is fundamental to deciphering when and how specific DNA repair and recombination processes are established and used. RPA–ssDNA complexes serve as binding targets for recruitment of the appropriate enzymes during various DNA metabolic processes, and physical interactions between RPA and more than two dozen enzymes have been identified. After recruitment, the bound ssDNA must be handed over from RPA or remodeled in such a way that the DNA is accessible to the incoming enzyme while RPA remains at the site. Microscopic binding and dissociation of the RPA DBDs is likely to enable the persistent residence of RPA at the site of repair as well as its ability to coordinate access to the DNA by helicases and nucleases. Such a mechanism might also be applicable to RPA-like proteins that also carry a multi-oligonucleotide/oligosaccharide-binding fold architecture, such as the CST complex associated with telomerase[40].

Methods

Chemicals and reagents

4-Azidophenylalanine (4-AZP) was prepared from Fmoc-4-amino-phenylalanine (Angene Inc.) as described[19]. All fluorophores used to generate fluorescently labeled proteins were purchased from Click Chemistry Tools. Cy3-labeled, biotinylated and unmodified oligonucleotides were purchased form Integrated DNA Technologies.

Plasmids and protein expression

Plasmids used in this study are detailed in Supplementary Note [3]. *S. cerevisiae* RPA was purified and fluorescently labeled as described[19]. Minor modifications to the published procedure are described in Supplementary Note [3]. *S. cerevisiae* Rad52 was purified as described[18] with the modifications as detailed in Supplementary Note [3]. Site-specific incorporation of 4-AZP was confirmed via MS analysis (Supplementary Dataset 7).

Generation of fluorescently labeled RPA variants

RPA variants carrying 4-AZP were labeled with MB543, Cy3 or Cy5 as previously described[19] with the following modifications. Briefly, ~3 ml of RPA^{4-AZP} (10 µM) was incubated on a rocker with a 1.5-fold molar excess (15 µM) of dibenzocyclooctyne-amine fluorophore (DBCO-MB543, DBCO-Cy3 or DBCO-Cy5) for 2 h at 4 °C. Labeled RPA variants were separated from excess dye using a Biogel-P4 gel filtration column (Bio-Rad Laboratories; 65 ml bed volume) using a storage buffer (30 mM HEPES, pH 7.8, 100 mM KCl and 10% (v/v) glycerol). Fractions containing labeled RPA were pooled, concentrated using a 30-kDa cut-off spin concentrator and flash-frozen using liquid nitrogen. Fluorescent RPA was stored at −80 °C. Labeling efficiency was calculated using the respective extinction coefficients (ε) and absorption values measured at 280 nm, with ε_{280} = 98,500 $M^{-1} cm^{-1}$ for RPA, at 550 nm, with ε_{550} = 105,000 $M^{-1} cm^{-1}$ for DBCO-MB543, at 555 nm, with ε_{555} = 150,000 $M^{-1} cm^{-1}$ for DBCO-Cy3, and at 650 nm, with ε_{650} = 250,000 $M^{-1} cm^{-1}$ for DBCO-Cy5 fluorophores. We obtained 45 ± 17% and 40 ± 25% labeling efficiencies for the RPA–DBD-A^{MB543} and RPA–DBD-D^{MB543}, respectively.

Fluorescence measurements

Fluorescence spectra were obtained using a PTI QM40 instrument (Horiba Scientific). For RPA–DBD-A^{MB543}, RPA–DBD-A^{Cy5} and RPA–DBD-A^{Cy3}, slit widths were set at 1.25 nm for excitation and 3 nm for emission. For RPA–DBD-D^{Cy3} and RPA–DBD-D^{Cy5}, slit widths were set at 0.5 nm for excitation and 2 nm for emission. For RPA–DBD-A^{MB543}, 2 ml of 50 nM RPA-A^{MB543} in reaction buffer (30 mM HEPES, pH 7.8, 100 mM KCl, 5 mM MgCl$_2$, 1 mM β-mercaptoethanol and 6% v/v glycerol) was added to a quartz cuvette, and the spectra were collected in the absence or presence of 50 nM ssDNA((dT)$_{45}$) or double-stranded plasmid DNA (100 nM nucleotides) with constant stirring. Samples were excited at 535 nm, and emission spectra (555–600 nm) were recorded. A similar experimental setup was used to obtain fluorescence spectra for 50 nM RPA–FAB^{MB543} after the addition of 100 nM (dT)$_{45}$. For RPA–DBD-D^{Cy3} and RPA–DBD-A^{Cy3}, 2 ml of 100 nM protein was used and 100 nM of (dT)$_{45}$ was added with constant stirring. The samples were excited at 559 nm, and emission spectra (539–579 nm) were recorded. Similarly, for RPA–DBD-A^{Cy5} and RPA–DBD-D^{Cy5}, 2 ml of 100 nM proteins were used and 100 nM of (dT)$_{45}$ was added to the reaction. Samples were excited at 690 nm, and emission spectra (640–700 nm) were recorded. All experiments were performed at 25 °C. The total number of nucleotides occupied (site size) by wild-type (wt) RPA and its variants (RPA-wt, RPA–DBD-A^{MB543} and RPA–DBD-D^{MB543}) in reaction buffer was determined as previously described using poly(dT) ssDNA[22].

DNA binding

The DNA-binding activity of unlabeled and fluorescent RPA was measured using electromobility band-shift analysis. 50 nM of ^{32}P-labeled (dT)$_{30}$ oligonucleotide was incubated with increasing concentrations of RPA-wt or RPA–DBD-A^{MB543} or RPA–DBD-D^{MB543} (0–1 µM) in reaction buffer for 10 min at 4 °C. 1 ml of DNA loading dye (50% v/v glycerol and 0.2% w/v bromophenol blue in 1×Tris–borate–EDTA (TBE) buffer) was added to the samples and samples were resolved using an 8% TBE–acrylamide gel (110 V, 25 °C). Gels were exposed overnight onto a phosphorimaging screen and scanned using a STORM scanner (GE Healthcare). Bound and unbound DNA signals were quantitated using ImageQuant software, and the fraction of ssDNA bound to RPA was calculated using the equation

$$((\text{bound } ^{32}\text{Psignal})/(\text{bound } ^{32}\text{Psignal} + \text{unbound } ^{32}\text{Psignal})) \times [\text{ssDNA}] \text{ (1)}$$

Stopped-flow analysis of RPA–DNA interactions

The stopped-flow experiments described below to monitor RPA–ssDNA dynamics were performed using an Applied Photophysics SX20 instrument in reaction buffer (30 mM HEPES, pH 7.8, 100 mM KCl, 5 mM MgCl$_2$, 1 mM β-mercaptoethanol and 6% v/v glycerol) at 25 °C. All the concentrations mentioned here are pre-mixing concentrations, which are reduced to half after mixture of the samples to provide final post-mixing concentrations. RPA labeled with MB543 was excited at 535 nm, and emission was monitored using a 555-nm cut-off filter (Newport Corp.). Changes in tryptophan fluorescence were monitored by exciting the samples at 290 nm, and emission was measured using a 350-nm cut-off filter. For the FRET experiments, the Cy5-labeled RPA and Cy3-labeled DNA samples were mixed and excited at 555 nm, and changes in Cy5 fluorescence were monitored with a 645-nm cut-off emission filter.

RPA–DBD-A$^{\text{MB543}}$, RPA–DBD-D$^{\text{MB543}}$ and RPA–FAB$^{\text{MB543}}$ ssDNA-binding kinetics

To quantitate the binding of RPA–DBD-A$^{\text{MB543}}$, RPA–DBD-D$^{\text{MB543}}$ or RPA to ssDNA, 200 nM of the respective protein was rapidly mixed with 200 nm of $(dT)_{25}$ oligonucleotide, and the change in MB543 fluorescence was captured. All the data were fitted using Kintek Explorer to obtain the appropriate rate constants. For RPA–DBD-A$^{\text{MB543}}$, the data were fit using a phenomenological double exponential plus linear equation:

$$\Delta f = A_1(1 - e^{-k_1 t}) + A_2(1 - e^{-k_2 t}) + k_3 t \text{ (2)}$$

where Δf is the change in fluorescence signal, A_1 and A_2 are the amplitude of fluorescence change, k_1, k_2 and k_3 are the observed rate constants and t is time. For RPA–DBD-D$^{\text{MB543}}$ and RPA–FAB$^{\text{MB543}}$, the data were well described by a single-step binding model defined phenomenologically by a single exponential plus linear equation

$$\Delta f = A_1(1 - e^{-k_1 t}) + k_2 t \text{ (3)}$$

RPA–DBD-A$^{\text{MB543}}$, RPA–DBD-D$^{\text{MB543}}$ and RPA–FAB$^{\text{MB543}}$ association kinetics

To obtain the rate of association for DBD-A binding to ssDNA, 200 nM RPA-A$^{\text{MB543}}$ in one syringe was rapidly mixed with increasing concentrations (50–400 nM) of $(dT)_{35}$ oligonucleotide from a second syringe, and the change in fluorescence of RPA–DBD-A$^{\text{MB543}}$ was monitored. All the data obtained were analyzed using equation (2) to obtain observed rate constants. Then, $k_{\text{obs},1}$ was plotted against the concentration of $(dT)_{35}$, and a linear fit was used to generate a rate for the binding of DBD-A to ssDNA. Similarly, to measure the binding of DBD-D to ssDNA, 200 nM RPA–DBD-D$^{\text{MB543}}$ in one syringe was rapidly mixed with increasing concentrations (50–400 nM) of $(dT)_{35}$ oligonucleotide from a second syringe, and the change in fluorescence of RPA-D$^{\text{MB543}}$ was monitored. Finally, to obtain the rate of association of FAB binding to ssDNA, 300 nM FAB$^{\text{MB543}}$ in one syringe was rapidly mixed with increasing concentrations (100–1000 nM) of $(dT)_{30}$ oligonucleotide from a second syringe, and the change in fluorescence of FAB$^{\text{MB543}}$ was monitored. For RPA–DBD-D$^{\text{MB543}}$ and RPA–FAB$^{\text{MB543}}$, all the data obtained were analyzed using equation (3) to obtain the observed rate constants. Then, $k_{\text{obs},1}$ was plotted against the concentration of $(dT)_{35}$ and against that of $(dT)_{30}$ for RPA–DBD-D$^{\text{MB543}}$ and RPA–FAB$^{\text{MB543}}$, respectively. A linear fit was used to generate a rate for the binding of DBD-D and FAB to ssDNA.

RPA-A^{MB543} and RPA-D^{MB543} length-dependent association kinetics

To measure the oligonucleotide length-dependent rate of association for DBD-A, 200 nM RPA–DBD-A^{MB543} was rapidly mixed with 200 nM (dT)$_8$, (dT)$_{10}$, (dT)$_{15}$, (dT)$_{20}$, (dT)$_{25}$, (dT)$_{30}$ or (dT)$_{35}$, and the change in fluorescence was monitored. All the data obtained were analyzed using equation (2) to obtain the observed rates. Then $k_{obs,1}$ was plotted against (dT)$_n$ to determine the rate for the oligonucleotide-length-dependent association of DBD-A. Using the same concentration of reactants, similar experiments were performed with RPA–DBD-D^{MB543} and RPA–FAB^{MB543} to measure the oligonucleotide-length-dependent rate of association for DBD-D. All the data obtained were analyzed using equation (3) to obtain the observed rates. Then, $k_{obs,1}$ was plotted against (dT)$_n$ to determine the rate for the oligonucleotide-length-dependent association of FAB and DBD-D.

RPA–DBD-A^{Cy5} and RPA–DBD-D^{Cy5} polarity for DNA binding

For all FRET experiments, samples (Cy3) were excited at 555 nm, and Cy5 fluorescence emission was monitored with a 645-nm long-pass emission filter. 5'- or 3'-Cy3-labeled DNA (100 nM) was mixed with the appropriate Cy5-labeled RPA protein, and the change in Cy5 fluorescence was captured. Data were fit to equation (3) to obtain observed rate constants for the resulting change in fluorescence.

RPA–DBD-A^{MB543} and RPA–DBD-D^{MB543} facilitated exchange kinetics

200 nM RPA–DBD-A^{MB543} or RPA–DBD-A^{MB543} was premixed with 200 nM (dT)$_{25}$ in one syringe to form the RPA–DNA complex and was rapidly mixed with increasing concentrations of RPA-wt from a second syringe (100–500 nM). The change in MB543 fluorescence was monitored, and the data were analyzed using equation (3) to obtain the observed rate constants. Then, $k_{obs,1}$ was plotted against the concentration of RPA-wt, and a linear fit was used to generate a rate for the facilitated exchange processes.

RPA–FAB^{MB543} facilitated exchange kinetics

To measure the facilitated exchange kinetics of FAB^{MB543}, FAB^{MB543}–(dT)$_{30}$ complexes were pre-formed using 375 nM FAB^{MB543} and 100 nM (dT)$_{30}$ in one syringe. FAB^{MB543}–(dT)$_{30}$ complexes were rapidly mixed with increasing concentrations of RPA-wt from a second syringe (100–500 nM), and the change in fluorescence of FAB^{MB543} was monitored. All the data obtained were analyzed using equation (3) to obtain the observed rate constants. Then $k_{obs,1}$ was plotted against the concentration of RPA-wt, and a linear fit was used to generate a rate for the facilitated exchange processes.

Tryptophan binding kinetics

Intrinsic tryptophan fluorescence was used to capture the binding of unlabeled and fluorescently labeled RPA variants to ssDNA in reaction buffer. 200 nM RPA (RPA-wt, RPA–DBD-A^{MB543} or RPA–DBD-D^{MB543}) was rapidly mixed with increasing concentrations (50–400 nM) of (dT)$_{35}$ oligonucleotide, and the change in Trp fluorescence was monitored by exciting the sample at 290 nm and measuring emission with a 350-nm cut-off filter. Data were fit using equation (3), and $k_{obs,1}$ was plotted against the concentration of (dT)$_{35}$. A linear fit was used to obtain the observed rate constants for RPA–DNA binding.

Single-molecule imaging

A custom-built prism-type total internal reflection microscope was used for all single-molecule experiments. A diode-pumped solid-state green laser (532 nm, Coherent) was used to excite the MB543 dye. The laser power output was set to 45 mW at the entrance to the microscope stage, unless otherwise noted. A dual-band-pass filter (Semrock; FF01–577/690) was used to filter out scattered light in the emission optical path, and the MB543 fluorescence was collected using a Chroma ET605/70m filter. Videos were recorded using an electron-multiplying charge-coupled device camera (Andor; DU-897-E-CSO-#BV) at 100-ms time resolution. Background was set to 400, correction was set to 1,200 and gain was set to 295 for all videos recorded.

FRET-based assays for Rad52 inhibition

Epigallocatechin (EGC, Sigma-Aldrich) has been previously characterized as an inhibitor of human RAD52–ssDNA binding[35]. To verify that EGC also inhibits the ssDNA binding of *S. cerevisiae* Rad52 but not *S. cerevisiae* RPA, we carried out FRET-based inhibitor assays as described[35]. A Cary Eclipse spectrofluorimeter was used to monitor the Cy3 and Cy5 emission simultaneously. Cy3 was excited at 530 nm, and emission was collected at 565 nm with slit widths of 10 nm. Cy5 was excited through FRET transfer with Cy3, and emission was collected at 660 nm with a slit width of 10 nm. Experiments were performed at 37 °C in a buffer containing 50 mM Tris-HCl, pH 7.5, 5 mM MgCl, 100 mM NaCl, 1 mM DTT and 0.1 mg ml^{-1} BSA.

EGC's inhibition of Rad52–ssDNA binding was tested by pre-mixing 100 nM Rad52 and 10 nM Cy3-dT30-Cy5 ssDNA to form a stoichiometric complex, which corresponds to ssDNA fully wrapped around the oligomeric Rad52 ring and, correspondingly, the high FRET state[41], and titrating increasing concentrations of EGC. Experiments were carried out in triplicate, and FRET signal and median inhibitory concentration were calculated as previously described[35].

EGC's inhibition of RPA–ssDNA binding was tested by pre-mixing 10 nM RPA and 10 nM Cy3-dT30-Cy5 ssDNA to form a stoichiometric complex in which the DNA is straightened to its contour length[41], and titrating increasing concentrations of EGC. Experiments were carried out in triplicate, and the FRET signal was calculated as described above.

Single-molecule cell assembly

Slides were washed, coated and flow cell assembled as described previously[42]. Reaction buffer containing 50 mM Tris-HCl, pH 7.5, 5 mM MgCl, 100 mM NaCl, 1 mM DTT, 0.1 mg ml^{-1} BSA and 0.8% glucose in Trolox was used for all single-molecule experiments. 12 mM Trolox (6-hydroxy-2,5,7,8-tetramethylchromane-2-carboxylic acid, Sigma-Aldrich; 238813-1G) was dissolved in 12 mM NaOH and was rotated under a fluorescent light (Sylvaia FM13W/835) for 3 days or until the absorbance at 400 nm was approximately 0.119. Assembled flow cells were first rinsed with T50 (10 mM Tris-HCl, pH 7.5, and 50 mM NaCl), then were incubated with 0.2 mg ml^{-1} NeutrAvidin (Thermo Fisher) for 3 min and then rinsed with T50 again.

Single-molecule experiments

To tether ssDNA to the slide surface, the flow cell was incubated for 3 min with 100 pM biotinylated 66-nt oligonucleotide (/5Biosg/ CTC AAG CCA TCC GCA ACG TTT TTT TTT TTT TTT TTT TTT TTT TTT TTT GAA ACA AAG GGC TCC TCA; IDT) in reaction buffer, then rinsed with reaction buffer. 2,100-frame, 210-s videos were recorded with 100 pM RPA–DBD-A^{MB543} or RPA–DBD-D^{MB543} added after the first 300 frames. At 1,200 frames, free RPA was either washed away with reaction buffer or replaced with 700 pM Rad52.

Experiments with RPA–FAB-A^{MB543} were carried out as described above, except 1 nM RPA–FAB-A^{MB543} was added at 300 frames with no wash. The experiment with human RAD52 was carried out as described, adding 700 pM human RAD52 instead of *S. cerevisiae* Rad52. EGC inhibitor single-molecule experiments were carried out as for the addition of Rad52 to RPA–DBD-D^{MB543} described above, with the addition of 10 M EGC premixed with Rad52 in reaction buffer. To challenge RPA binding to ssDNA, experiments were performed with 1 nM of a 42-nt unlabeled ssDNA oligonucleotide (5'-TTT TTT TTT TTT TTT TTT TTG GAA TTA AGC TCT AAG CCA TCC-3') added to the reaction buffer in the wash step.

Except where indicated otherwise, the excitation laser power was set to 45 mW at the entrance to the microscope stage. Laser power experiments were performed as described above, but at 36 and 27 mW, and results were then compared to previous experiments carried out at maximum laser power (45 mW) of the green laser (532 nm).

Surface-tethered RPA

RPA–DBD-D^{MB543} contains a polyhistidine tag on the C terminus of RPA32, which was used to tether the protein to the slide surface. The slide was first incubated with NeutrAvidin and rinsed and was then incubated with Biotin-X-NTA buffer (50 mM Tris, pH 7.5, 50 mM NaCl and 20 nM Biotin-X-NTA, Sigma-Aldrich) for 10 min. The same reaction buffer was used, with the addition of 5 µM NiSO$_4$. The chamber was rinsed with reaction buffer, followed by the addition of 500 pM RPA–DBD-D^{MB543}, which was incubated in the chamber for 5 min. The chamber was then rinsed with reaction buffer. A 2,100-frame, 210-s video was recorded.

Single-molecule data analysis

An IDL script was used to extract fluorescence intensity trajectories (changes in the fluorescence over time in a particular location on the flow cell) from each video (available upon request). Only those trajectories that show the appearance of the fluorescence signal between 30 s and 120 s (indicated as ON in Fig. 3c,d) were selected for analysis. Traces were viewed using a Matlab script and were selected using the following three criteria: at least two transitions, signal-to-noise ratio > 4 (raw signal), and no signal before addition of a fluorophore. Traces that did not meet these criteria were discarded.

The selected traces were then saved individually and processed for analysis by ebFRET[27,43] Since ebFRET was developed to analyze two-channel trajectories, where recorded donor and acceptor fluorescence is recalculated into FRET efficiency, which is between 0 and 1, our single-color trajectories required normalization before analysis. To prepare fluorescence trajectories for the analysis by ebFRET, we used emulateFRET, a program that normalizes intensity in all experimental trajectories to be within the range of 0 to 1 (Supplementary Fig. 5). Fluorescent trajectories were imported into emulateFRET in batches and analyzed as a group. A percentile calculation determined a threshold for the maximum intensity in the group while excluding outliers. For each trajectory, the fluorescence in each point was then divided by this maximum intensity. This all traces to the range from 0 to 1. A weighted moving-average algorithm (of width 5) removed a small amount of noise in each trajectory. For each trajectory, a histogram of the values in the trace was produced (a histogram of fluorescence intensity values binned in intervals of 5 units was shown on the right of the raw trajectory in a light green color, and a brighter green histogram with overlapping Gaussian curve represented the baseline values for the first 30 s before the addition of fluorescent RPA). This histogram showed a characteristic peak surrounding the values that comprise the baseline of that trajectory. The shape of this peak on the histogram was fit to a Gaussian distribution. From this Gaussian distribution, the new baseline was determined and was placed 2 s.d. above the mean of this peak. All values below this baseline were reassigned to surround the new baseline value. This suppressed the ebFRET program's tendency to assign multiple states to the typically over-represented baseline signal. The edited trajectories were given a dummy 'donor' trace, calculated such that the FRET signal of each pair was equal to the normalized input trace. Each pair of normalized trajectories was then exported to the file format that ebFRET uses to import raw donor and acceptor values. The converted ebFRET compatible traces were then trimmed to exclude portions of the recording before the addition of fluorescent material. The trimmed traces were loaded into the ebFRET MatLab program. Analysis was carried out for 2 to 5 states, with 10 repeats and a precision of $10e^{-06}$.

After normalization, trajectories from Rad52 addition versus buffer experiments were trimmed to include separate portions of the experiment: 300–1,200 frames after RPA addition, and 1,200–2,100 frames after Rad52 or buffer addition. Each portion was analyzed separately using ebFRET. The output from ebFRET was then analyzed by KERA v3.0 to sort dwell times of individual events at each state. The dwell times were binned with the first center at 400 ms with a width of each bin of 300 ms. The dwell times were fit to one- and two-phase exponential decays using GraphPad Prism v7.03. The *F*-test suggested that single exponential decay was the best fit for dwell-time distributions.

Several modifications were introduced to analyze the data from the surface-tethered RPA. Trajectories were selected for analysis only when (1) there was no signal in the 'red' channel, (2) fluorescence terminated in a single-step photobleaching event at least 30 s before the end of the recording, and (3) the signal-to-noise ratio was >4. Selected trajectories were normalized using emulateFRET with the baseline selected as the portion occurring after photobleaching (final 30 s of the video). After normalization, the trajectories were trimmed at 10 s after photobleaching. Normalized trajectories were analyzed using ebFRET as previously described for the surface-tethered ssDNA.

S. cerevisiae Rad52 versus human RAD52 electrophoretic mobility-shift assay (EMSA)

A Cy5-labeled 30-nt ssDNA substrate (TGC ATA TCA GAT GCC TCG CGT CCG TCG CCA /Cy5/) was used in the EMSA. Reactions were prepared in KPi buffer (30 mM Kpi (pH 7.4), 5 mM MgCl, 100 mM NaCl, 1 mM DTT and 0.01 mg ml^{-1} BSA). Increasing concentrations of *S. cerevisiae* Rad52 or human RAD52 (50 nM, 150 nM, 500 nM and 1,000 nM) were added to 10 nM ssDNA coated with *S. cerevisiae* RPA (100 nM). Controls with free ssDNA (10 nM ssDNA), RPA-coated DNA (100 nM RPA) and Rad52 on RPA-free DNA (1,000 nM Rad52) were also prepared. The samples were split in half, and one half was crosslinked with 0.01% glutaraldehyde. Samples were incubated at 37 °C for 5 min. Samples were loaded on to 1% agarose gel with 10×orange loading dye (TAE, 30% glycerol and 4 mg ml^{-1} Orange G). The agarose gel was then run at room temperature for 1 h at 50 V. A Bio-Rad ChemiDoc MP Imaging System was used to image the gel using a Cy5 protocol.

Reporting Summary

Further information on research design is available in the Nature Research Reporting Summary linked to this article.

Data availability

The data supporting the conclusions of this study are presented in Supplementary Datasets 1–7. Source data for Figs. 1–4, 6, 7 and 9 are available online. Additional data, plasmids for protein expression and code for single-molecule data analysis are available from the corresponding authors upon request.

References

1. Chen, R. & Wold, M. S. Replication protein A: single-stranded DNA's first responder: dynamic DNA-interactions allow replication protein A to direct single-strand DNA intermediates into different pathways for synthesis or repair. *BioEssays* **36**, 1156–1161 (2014).
2. Wold, M. S. Replication protein A: a heterotrimeric, single-stranded DNA-binding protein required for eukaryotic DNA metabolism. *Annu. Rev. Biochem.* **66**, 61–92 (1997).
3. Fanning, E., Klimovich, V. & Nager, A. R. A dynamic model for replication protein A (RPA) function in DNA processing pathways. *Nucleic Acids Res.* **34**, 4126–4137 (2006).
4. Nguyen, B. et al. Diffusion of human replication protein A along single-stranded DNA. *J. Mol. Biol.* **426**, 3246–3261 (2014).
5. Gibb, B. et al. Concentration-dependent exchange of replication protein A on single-stranded DNA revealed by single-molecule imaging. *PLoS ONE* **9**, e87922 (2014).
6. Chen, R., Subramanyam, S., Elcock, A. H., Spies, M. & Wold, M. S. Dynamic binding of replication protein a is required for DNA repair. *Nucleic Acids Res.* **44**, 5758–5772 (2016).
7. Arunkumar, A. I., Stauffer, M. E., Bochkareva, E., Bochkarev, A. & Chazin, W. J. Independent and coordinated functions of replication protein A tandem high affinity single-stranded DNA binding domains. *J. Biol. Chem.* **278**, 41077–41082 (2003).
8. Bochkareva, E., Korolev, S., Lees-Miller, S. P. & Bochkarev, A. Structure of the RPA trimerization core and its role in the multistep DNA-binding mechanism of RPA. *EMBO J.* **21**, 1855–1863 (2002).

9. Wyka, I. M., Dhar, K., Binz, S. K. & Wold, M. S. Replication protein A interactions with DNA: differential binding of the core domains and analysis of the DNA interaction surface. *Biochemistry* **42**, 12909–12918 (2003).

10. Bochkareva, E., Frappier, L., Edwards, A. M. & Bochkarev, A. The RPA32 subunit of human replication protein A contains a single-stranded DNA-binding domain. *J. Biol. Chem.* **273**, 3932–3936 (1998).

11. Bastin-Shanower, S. A. & Brill, S. J. Functional analysis of the four DNA binding domains of replication protein A. The role of RPA2 in ssDNA binding. *J. Biol. Chem.* **276**, 36446–36453 (2001).

12. Fan, J. & Pavletich, N. P. Structure and conformational change of a replication protein A heterotrimer bound to ssDNA. *Genes Dev.* **26**, 2337–2347 (2012).

13. Benson, F. E., Baumann, P. & West, S. C. Synergistic actions of Rad51 and Rad52 in recombination and DNA repair. *Nature* **391**, 401–404 (1998).

14. Shinohara, A. & Ogawa, T. Stimulation by Rad52 of yeast Rad51-mediated recombination. *Nature* **391**, 404–407 (1998).

15. New, J. H., Sugiyama, T., Zaitseva, E. & Kowalczykowski, S. C. Rad52 protein stimulates DNA strand exchange by Rad51 and replication protein A. *Nature* **391**, 407–410 (1998).

16. Sung, P. Function of yeast Rad52 protein as a mediator between replication protein A and the Rad51 recombinase. *J. Biol. Chem.* **272**, 28194–28197 (1997).

17. Sugiyama, T. & Kowalczykowski, S. C. Rad52 protein associates with replication protein A (RPA)-single-stranded DNA to accelerate Rad51-mediated displacement of RPA and presynaptic complex formation. *J. Biol. Chem.* **277**, 31663–31672 (2002).

18. Gibb, B. et al. Protein dynamics during presynaptic-complex assembly on individual single-stranded DNA molecules. *Nat. Struct. Mol. Biol.* **21**, 893–900 (2014).

19. Pokhrel, N. et al. Monitoring replication protein a (RPA) dynamics in homologous recombination through site-specific incorporation of non-canonical amino acids. *Nucleic Acids Res.* **45**, 9413–9426 (2017).

20. Brosey, C. A. et al. Functional dynamics in replication protein A DNA binding and protein recruitment domains. *Structure* **23**, 1028–1038 (2015).

21. Brosey, C. A. et al. A new structural framework for integrating replication protein A into DNA processing machinery. *Nucleic Acids Res.* **41**, 2313–2327 (2013).

22. Kumaran, S., Kozlov, A. G. & Lohman, T. M. *Saccharomyces cerevisiae* replication protein A binds to single-stranded DNA in multiple salt-dependent modes. *Biochemistry* **45**, 11958–11973 (2006).

23. Kolpashchikov, D. M. et al. Polarity of human replication protein A binding to DNA. *Nucleic Acids Res.* **29**, 373–379 (2001).

24. Brosey, C. A. et al. NMR analysis of the architecture and functional remodeling of a modular multidomain protein, RPA. *J. Am. Chem. Soc.* **131**, 6346–6347 (2009).

25. Boehm, E. M., Subramanyam, S., Ghoneim, M., Washington, M. T. & Spies, M. Quantifying the assembly of multicomponent molecular machines by single-molecule total internal reflection fluorescence microscopy. *Methods Enzymol.* **581**, 105–145 (2016).

26. Ghoneim, M. & Spies, M. Direct correlation of DNA binding and single protein domain motion via dual illumination fluorescence microscopy. *Nano Lett.* **14**, 5920–5931 (2014).

27. Van de Meent, J.-W., Bronson, J. E., Wiggins, C. H. & Gonzalez, R. L. Jr. Empirical Bayes methods enable advanced population-level analyses of single-molecule FRET experiments. *Biophys. J.* **106**, 1327–1337 (2014).

28. Subramanyam, S., Kinz-Thompson, C. D., Gonzalez, R. L. Jr & Spies, M. Observation and analysis of rad51 nucleation dynamics at single-monomer resolution. *Methods Enzymol.* **600**, 201–232 (2018).

29. Lu, H. P. & Xie, X. S. Single-molecule spectral fluctuations at room temperature. *Nature* **385**, 143–146 (1997).

30. Brender, J. R. et al. Conformational dynamics of the isoalloxazine in substrate-free p-hydroxybenzoate hydroxylase: single-molecule studies. *J. Am. Chem. Soc.* **127**, 18171–18178 (2005).

31. Pretto, D. I. et al. Structural dynamics and single-stranded DNA binding activity of the three N-terminal domains of the large subunit of replication protein A from small angle X-ray scattering. *Biochemistry* **49**, 2880–2889 (2010).

32. Plate, I. et al. Interaction with RPA is necessary for Rad52 repair center formation and for its mediator activity. *J. Biol. Chem.* **283**, 29077–29085 (2008).
33. Seong, C. et al. Molecular anatomy of the recombination mediator function of *Saccharomyces cerevisiae* Rad52. *J. Biol. Chem.* **283**, 12166–12174 (2008).
34. Sugiyama, T., New, J. H. & Kowalczykowski, S. C. DNA annealing by RAD52 protein is stimulated by specific interaction with the complex of replication protein A and single-stranded DNA. *Proc. Natl Acad. Sci. USA* **95**, 6049–6054 (1998).
35. Hengel, S. R. et al. Small-molecule inhibitors identify the RAD52-ssDNA interaction as critical for recovery from replication stress and for survival of BRCA2 deficient cells. *eLife* **5**, e14740 (2016).
36. Sugiyama, T. & Kantake, N. Dynamic regulatory interactions of rad51, rad52, and replication protein-a in recombination intermediates. *J. Mol. Biol.* **390**, 45–55 (2009).
37. Qiu, Y. et al. Srs2 prevents Rad51 filament formation by repetitive motion on DNA. *Nat. Commun.* **4**, 2281 (2013).
38. Subramanyam, S., Ismail, M., Bhattacharya, I. & Spies, M. Tyrosine phosphorylation stimulates activity of human RAD51 recombinase through altered nucleoprotein filament dynamics. *Proc. Natl Acad. Sci. USA* **113**, E6045–E6054 (2016).
39. Candelli, A. et al. Visualization and quantification of nascent RAD51 filament formation at single-monomer resolution. *Proc. Natl Acad. Sci. USA* **111**, 15090–15095 (2014).
40. Chan, H., Wang, Y. & Feigon, J. Progress in human and tetrahymena telomerase structure determination. *Annu. Rev. Biophys.* **46**, 199–225 (2017).
41. Grimme, J. M. & Spies, M. FRET-based assays to monitor DNA binding and annealing by Rad52 recombination mediator protein. *Methods Mol. Biol.* **745**, 463–483 (2011).
42. Bain, F. E., Wu, C. G. & Spies, M. Single-molecule sorting of DNA helicases. *Methods* **108**, 14–23 (2016).
43. Kinz-Thompson, C. D., Bailey, N. A. & Gonzalez, R. L. Jr. Precisely and accurately inferring single-molecule rate constants. *Methods Enzymol.* **581**, 187–225 (2016).

Acknowledgements

Author information

Author notes

These authors contributed equally: Nilisha Pokhrel, Colleen C. Caldwell.

Affiliations

Department of Biological Sciences, Marquette University, Milwaukee, WI, USA

Nilisha Pokhrel, Elliot I. Corless, Emma A. Tillison & Edwin Antony

Department of Biochemistry, Carver College of Medicine, University of Iowa, Iowa City, IA, USA

Colleen C. Caldwell, Nina Jocic, Marc S. Wold & Maria Spies

Department of Physics, University of Northern Iowa, Cedar Falls, IA, USA

Joseph Tibbs, Nina Jocic & S. M. Ali Tabei

Contributions

Corresponding authors
Correspondence to Maria Spies or Edwin Antony.

Ethics declarations

Competing interests
The authors declare no competing interests.

Additional information

Publisher's note: Springer Nature remains neutral with regard to jurisdictional claims in published maps and institutional affiliations.

Integrated supplementary information

Supplementary Figure 1 DNA binding properties of fluorescent RPA.

Stopped flow experiments were performed by mixing **(a)** RPA-wt, **(b)** RPA-DBD-A^{MB543}or **(c)** RPA-DBD-D^{MB543} with increasing concentrations of ssDNA [(dT)$_{35}$], and the change in intrinsic tryptophan fluorescence was recorded. **(d-f)** Data were fit as described in *methods* to obtain k$_{off}$ and k$_{on}$ values, and the apparent K$_D$ values were calculated. **(g)** Stoichiometric binding of unlabeled or labeled versions of RPA to ^{32}P-labeled [(dT)$_{30}$] oligonucleotide (50 nM) is observed in EMSA experiments. **(h)** Occluded site-size measurements were performed by adding increasing concentrations of poly(dT) ssDNA to RPA (0.2 µM) and monitoring the change in tryptophan fluorescence. All versions of RPA occlude ~20 ± 2 nt/RPA in our reaction conditions (30 mM Hepes, pH 7.8, 100 mM KCl, 5 mM MgCl$_2$, 1 mM β-mercaptoethanol and 6 % v/v glycerol). These experiments show that the DNA binding properties of the labeled RPA are similar to the unlabeled wild type RPA complex.

Supplementary Figure 2 Spectral properties of fluorescent RPA and changes in MB543 fluorescence reflect conformational changes associated with electrostatic interactions.

(a) Structure of DBCO-MB543 used to fluorescently label RPA in this study. **(b)**Excitation and emission spectra of RPA-DBD-A^{MB543} in solution. **(c)** Percent change in fluorescence enhancement was measured for RPA-DBD-A^{MB543} in the absence or presence of ssDNA or **(d)** dsDNA. The change in fluorescence is specific for ssDNA interactions with RPA. **(e)** No change in fluorescence is observed for RPA-DBD-A^{Cy5}upon binding to ssDNA. Similar analysis for RPA-DBD-D^{MB543} were recently published (*Nucleic Acids Res*. **45**, 9413–9426, 2017). **(f)** The change in MB543 fluorescence was measured as a function of increasing concentrations of dimethyl formamide (DMF) or **(h)** ethanol, and **(g & i)** the respective change in fluorescence was plotted. The solvent dependent changes in emission spectra are suggestive of electrostatic changes around the fluorophore (*J. Photochem*. **3**, 55–69, 1974–1975).

Supplementary Figure 3 FRET experiments capture the polarity of RPA binding on ssDNA.

(a) & (c) Models of the expected FRET states and the polarity of the Cy5-DBD with respect to the Cy3-DNA. Boxes are color coded to match the traces in the data. Stopped flow experiments were performed by rapidly mixing either RPA-DBD-A^{Cy5} or RPA-DBD-D^{Cy5} with ssDNA labeled at the (b) 5' end or (d) 3' end with Cy3. Cy3 was excited and change in Cy5 emission was measured. The proximity of the Cy3 and Cy5 fluorophores dictate the observed FRET efficiency and results in the enhancement of Cy5 emission. Since RPA binds to ssDNA with a 5'→3' polarity, when RPA-DBD-A^{Cy5}resides close to the 5'Cy3 on DNA, a high FRET state is observed. Similarly, when RPA-DBD-D^{Cy5} binds close to the 3'Cy3, a high FRET signal is captured. k_{obs} values for change in FRET were obtained by fitting the data to a single exponential plus linear equation. Black traces are DNA only (no RPA). Pink and Green traces are experiments with RPA-DBD-A^{Cy5} and RPA-DBD-D^{Cy5}, respectively. The measured rates match well to the rates observed for RPA labeled with MB543 (Fig. 1e, f) suggesting that the ssDNA dependent changes in RPA-MB543 intensity reflect specific DBD-ssDNA interactions.

Supplementary Figure 4 The RPA fragment comprised of FAB domains displays rapid and monophasic binding to ssDNA and single-molecule analysis of RPA-FAB-A^{MB543}-ssDNA interaction reveal the presence of two distinct fluorescence states and more rapid dissociation than trimeric RPA-DBD-A^{MB543}.

The FAB region of RPA (DBDs F, A and B) was purified and labeled with MB543 at DBD-A (RPA-FAB-A^{MB543}), and (a) produces a robust change in fluorescence upon binding to ssDNA. (b) Stopped flow analysis shows rapid binding of RPA-FAB-A ^{MB543} (100 nM) to 100 nM of ssDNA of increasing lengths (dT)$_n$. A minimum of 15 nt is required to observe binding. (c) RPA-FAB-A^f binding dynamics on ssDNA were measured by monitoring the change in fluorescence upon binding to increasing concentrations of [(dT)$_{30}$] ssDNA. (d) Measurement of DNA binding kinetics reveal k_{on} (1.1±0.1 × 10^8 M^{-1}s^{-1}). The RPA-FAB-A^{MB543} binding data were fit to a single exponential plus linear equation to obtain $k_{obs,1}$. (e) Experimental scheme for visualization of the binding and conformational dynamics of FAB. Binding of the fluorescently-labeled FAB (1.0, 0.75, 0.50 µM) to ssDNA (blue line) tethered to the surface of TIRFM flow cell (grey line) brings the MB543 fluorophore within the evanescent field and its excitation. NA – neutravidin, b – biotin. (f)Representative fluorescence trajectories depicting binding (appearance and disappearance of the signal) and conformational dynamics (change in fluorescence without FAB dissociation) of the individual RPA-FAB-A^{MB543} molecules labeled within the DBD-A. Purple lines represent normalized fluorescence. Black lines represent the results of ebFRET fitting of the experimental data to the three-state model (where state 1 is the off state, while states 2 and 3 are the two bound states with different fluorescent intensities). The levels for the respective states are indicated by dashed lines. The top trajectory is representative of the most commonly observed type with short binding events and rare transitions between fluorescence states. At each RPA-FAB-A^{MB543} concentration, we also observed several trajectories displaying long binding events as the bottom trajectory here. (g) The dissociation rate constant, $k_{off}$was determined from the decay rate of the on state dwell time (when trajectories were fitted with the two state model). The average at the three concentrations is shown with standard deviation. (h) The association rate, V_{on} was determined as the number of binding events observed in each experiment divided by the product of the observation time and the number of trajectories observed at 1 nM RPA-FAB-A^{MB543}. The association rate constant, k_{on} was determined by calculating the slope of the V_{on} dependence on RPA-FAB-A^{MB543} concentration. The equilibrium dissociation rate constant, K_d is the ratio of the two rate constants. All calculations accounted for the RPA-FAB-A^{MB543}labeling efficiency. Source Data

Supplementary Figure 5 Normalization of fluorescence trajectories.

Representative fluorescence trajectory before (a) and after (b) normalization using the emulateFRET program as described in the Methods section. Briefly, to normalize each trajectory we first computed the maximum non-outlying value in this trajectory, which is the 98th percentile value among the values within the trajectory. Each fluorescence value in the trajectory is divided by the maximum non-outlying value; it is further multiplied by a factor of .85 to ensure that the entire trace fits well within the 0–1 range. This resulting trajectory is smoothed

with a five-point moving average. Any values in the trace which are still above 1 (these are not expected to occur with any significant frequency) are normalized down to equal 1 (though if this occurs, a small amount of noise is added to these few points, to avoid the trajectory equaling exactly 1 at any point). The second step in normalization determines the location of the new baseline. A histogram of the values from all trajectories collected during the first 30 seconds of the experiment is constructed. This histogram should have a peak at the value at which the baselines center, with a deviation corresponding to the variation in that baseline. The point which is two standard deviations above the mean of this peak is considered the new baseline for the traces. All values in the trace below this value are cut off, and set equal to this new baseline. To avoid the baseline remaining precisely flat (causing over-fitting in ebFRET), a small amount of noise (magnitude .005, at the most) is added throughout the traces. This new set of trajectories is then saved in a format, which ebFRET can read.

Supplementary Figure 6 In the absence of ssDNA, RPA-DBD-D^{MB543}does not display transitions between fluorescence states; single-molecule analysis of yeast RPA dynamics at several different laser powers shows no trend in number of states, visitation of states, or off-rates at each state, thus ruling out a photophysical cause of fluorescence intensity changes.

To determine whether the four fluorescence states we observed for the ssDNA-bound RPA-DBD-D^{MB543} are the result of the protein-DNA interaction we tethered RPA-DBD-D^{MB543} to the surface and observed its fluorescence. (**a**) Experimental scheme for visualization of RPA-DBD-D^{MB543} tethered to the surface of the slide chamber via a 6X polyhistidine tag at the C-terminus of RPA32 bound by Biotin-X-NTA (Sigma Cat#51410). b-biotin, N-neutravidin. scRPA tethered to the surface via this immobilization scheme does not bind ssDNA. We believe this is caused by steric constraints of the protein attachment. (**b**) Representative fluorescence trajectories depicting the fluorescence of tethered RPA-DBD-D^{MB543}. The following rules were followed to ensure that we are analyzing trajectories originating from the single surface-tethered RPA-DBD-D^{MB543} molecules: selected trajectories (1) showed fluorescence only in the "green" channel and no fluorescence in the "red" channel, (2) terminated in a single-step photobleaching event prior to the last 30 seconds of the movie, and (3) had a signal-to-noise ratio >4. Selected trajectories were normalized similarly to those of the surface-tethered ssDNA except the region of the trajectory after the photobleaching event was used to establish the baseline. Normalized trajectories were fitted with ebFRET to reveal the presence of only two states, fluorescent and the baseline. Photobleaching events in each trajectory are indicated by black arrows while transitions to the dark state are represented by red arrows. The total fluorescent time (7850 frames) was totaled from the trajectories (24) as was the time in the dark state that was not photobleaching (67 frames). 0.85% of time before photobleaching was occupied by dark state fluorescence. Dark state transitions were seen in 5/24 trajectories. These relatively rare dark state transitions can be attributed to blinking. This blinking likely occurs with similarly low frequency in experiments where RPA is bound to ssDNA. (**c**) In order to verify that the four fluorescent states observed in our experiments were not a result of photophysical effects of the MB543 fluorophore, experiments were carried out at various laser powers. Published work from many groups including ours provides an avenue to distinguish the photophysical source of the fluorescence changes from the actual conformational changes resulting in the change in the dye's environment [8-10]. This is especially important for the low intensity states that can be confused with the dye blinking, such as our state 1. The life times of the photophysical states of the dye should depend on the excitation laser power, while the true conformational states should be independent of it. Blinking frequency is also expected to change with the changing in the power of excitation laser. Experiments were carried out as described in Figure 3b with RPA-DBD-D^{MB543} in triplicate at three different laser powers (27, 36, and 45mW). Data for each independent experiment is plotted separately. Comparison of the fractional visitation to each state available to RPA-DBD-D^{MB543} with laser power set to 27 mW (blue), 36 mW (grey), and 45 mW (black). (**d**) Comparison of the stability of each state available to RPA-DBD-D^{MB543} at 27 mW (blue), 36 mW (grey), and 45 mW (black). The data on Y axis are the lifetimes calculated from the respective dwell time distributions. Data for each independent experiment is plotted separately. The life times and visitation frequencies for all states were

within an experimental error from one laser power to another suggesting that these states are not photophysical. Source Data

Supplementary Figure 7 Scavenger ssDNA in the buffer-wash step confirms that RPA-DBD-D^{MB543} remains bound to ssDNA in observed dark-state events.

In order to verify that the dark fluorescent state that is observed when excess RPA is washed away reflects a dimmer state of RPA-DBD-D^{MB543} still associated with DNA, we challenged the reaction with excess ssDNA. The free DNA in the reaction chamber is used as a scavenger, which would bind any RPA that dissociated, preventing reassociation, but should not strip the bound RPA from surface-tethered ssDNA[5]. **(a)**Experimental scheme for visualization of the effect of excess ssDNA on the RPA-DBD-D^{MB543} dynamics and association with DNA. Binding of the RPA-DBD-D^{MB543} (100pM) to the surface-tethered ssDNA (blue line) brings the MB543 fluorophore within the evanescent field and its excitation. 1nM ssDNA (42nt) was added at 90s when excess RPA was washed away. NA – neutravidin, b – biotin. **(b)** Representative fluorescence trajectories depicting the conformational dynamics of the individual RPA-DBD-D^{MB543}molecules. After replacement of RPA in the reaction chamber with 1nM ssDNA, the same four conformational states are observed in the RPA-DBD-D^{MB543} trajectories. As seen in experiments where excess RPA was washed away with reaction buffer, reappearance of higher fluorescence states are observed after visitation of the dark state (state 1) in the presence of excess ssDNA. RPA that dissociated would have been bound by the excess free DNA, thus indicating that the reappearance of higher fluorescence states (2,3,4) is due to RPA remaining bound while in the dark state (1) **(c)**Comparison of the stability of each state available to RPA-DBD-D^{MB543} when excess RPA is washed away with reaction buffer (grey) or reaction buffer containing 1nM ssDNA (blue). The data on Y axis are the lifetimes calculated from the respective dwell time distributions. Data for each independent experiment is plotted separately. **(d)**Comparison of the fractional visitation to each state available RPA-DBD-D^{MB543} when excess RPA is washed away with reaction buffer (grey) or reaction buffer containing 1nM ssDNA (blue). Source Data

Supplementary Figure 8 RPA-FAB is exchanged more readily on ssDNA compared to the full-length RPA.

(a-c) Preformed RPA-FAB-A^{MB543}:(dT)$_{25}$ complexes were challenged with increasing concentrations of unlabeled RPA-wt and the rate of exchange was measured by monitoring the decrease in fluorescence intensity. RPA-FAB-A^{MB543} was cleared at an apparent rate of ($1.3\pm0.3\times10^8$ M^{-1}s^{-1}). In comparison, **(d-h)** the rates of exchange of RPA-DBD-A^{MB543} or RPA-DBD-D^{MB543} by RPA-wt was two orders of magnitude slower.

Supplementary Figure 9 The importance of the physical interactions between RPA and Rad52 as well as Rad52 and ssDNA for the modulation of RPA domain dynamics.

The activities of the RAD52 on the RPA-coated ssDNA depend on the species-specific interaction between the two proteins [11]. To determine whether the physical interaction between Rad52 and RPA plays a role in the Rad52-mediated change in the RPA conformational dynamics, we carried out the single-molecule analysis of the yeast RPA dynamics in the presence of human RAD52. **(a)** Experimental scheme for visualization of the effect of hRAD52 on RPA-DBD-D dynamics. Binding of the fluorescently-labeled RPA (100pM) to the ssDNA (blue line) brings the MB543 fluorophore within the evanescent field and its excitation. NA – neutravidin, b – biotin. **(b)** Human RAD52 protein shares the conserved N-terminal domain with the yeast protein. This domain is responsible for the formation of the oligomeric ring and for the interaction with DNA. Their C-terminal, protein-protein interaction domains are highly different resulting in the absence of cross-species interactions with RPA. **(c)** Representative fluorescence trajectories depicting the conformational dynamics of the individual RPA molecules labeled within RPA-DBD-D. After replacement of RPA in the reaction chamber with 700pM hRAD52, the same four conformational states are observed in RPA-DBD-D^{MB543}trajectories suggesting that human RAD52 does not affect the yeast RPA conformational dynamics. Therefore, we conclude that the Rad52-RPA physical

interaction is required for the observed effect. **(d)**. Electrophoretic mobility shift assay (EMSA) of Cy5-labeled ssDNA (30nt) contrasting increasing concentrations of scRad52 vs hRAD52 added to scRPA coated ssDNA. Table includes reaction conditions for each lane. Reactions in the bottom portion were crosslinked using 0.1% glutaraldehyde. The species of each band are identified on the right of the gel. The results of this EMSA experiment suggest that the interaction between hRAD52 and scRPA-coated ssDNA are similar to that between scRad52 and the scRPA-coated ssDNA. Thus, the absence of the DBD-D modulation in the single-molecule control experiment is solemnly due to the absence of the protein-protein interaction between the ssDNA-bound scRPA and hRAD52. Previously, we identified epigallocatechin (EGC) as a specific inhibitor of the human RAD52 interaction with ssDNA [12]. In contract, EGC displays no activity towards human RPA [12]. Here, we confirmed that EGC also inhibits *S. cerevisiae* Rad52-ssDNA interaction and has no effect on the interaction between *S. cerevisiae* RPA and ssDNA. We therefore, used EGC to determine whether the interaction between Rad52 and ssDNA is important for the modulation of the RPA conformational dynamics. **(e)** FRET-based inhibitor titration of EGC into solution of 100 nM Rad52 and 10 nM Cy3-dT30-Cy5 ssDNA. FRET begins high where the FRET labeled DNA is wrapped around Rad52, bringing Cy3 and Cy5 into proximity and decreases as inhibitor prevents Rad52 ssDNA binding. The IC50 value calculated for inhibition of Rad52 ssDNA binding is shown below the curve. **(f)** FRET-based inhibitor titration of EGC into solution of 10 nM RPA and 10 nM Cy3-dT30-Cy5 ssDNA. The absence of FRET increase with EGC titration indicates that EGC does not inhibit RPA ssDNA binding. **(g)** Scheme depicting interactions between RPA and Rad52 and DNA. Addition of ECG inhibits Rad52 ssDNA binding. **(h)** Epigallocatechin (ECG), an inhibitor of Rad52 ssDNA binding. **(i)** Experimental scheme for visualization of the effect of Rad52 with 10uM EGC on RPA-DBD-D dynamics. Binding of the fluorescently-labeled RPA (100 pM) to the ssDNA (blue line) brings the MB543 fluorophore within the evanescent field and its excitation. NA – neutravidin, b – biotin. **(j)** Representative fluorescence trajectories depicting the conformational dynamics of the individual RPA molecules labeled within RPA-DBD-D. After replacement of RPA in the reaction chamber with 700 pM Rad52 and 10 uM EGC, the same four conformational states are observed in RPA-DBD-D^{MB543} trajectories. **(k)** Comparison of the lifetimes of the individual states and fractional visitation to each state available to RPA-DBD-D^{MB543} alone (grey) and in the presence of Rad52 (blue) and in the presence of Rad52 and EGC (red). Data from a single experiment was separated into three portions and each portion was analyzed and plotted separately. The presence of EGC returned almost all the lifetimes and all the visitation frequencies to the same values as were obtained in the absence of Rad52. Most importantly, we observed the reemergence of the state 4, suggesting that the Rad52-ssDNA interaction is important for the formation of the RPA-ssDNA-Rad52 complex that modulates the accessibility of the 3' ssDNA region occluded by RPA. A slight increase in the lifetime of the least fluorescent state 1 is likely the result of the interaction between Rad52 and RPA in the absence of the Rad52-ssDNA interaction. Source Data